THE JOURNAL OF PHYSICAL CHEMISTRY C
A JOURNAL OF THE AMERICAN CHEMICAL SOCIETY

pubs.acs.org/JPCC

Article

Durability of Colloidally Stabilized Supported Nickel and Nickel Platinum Nanoparticles during Redox-Cycling

Vivien Gutknecht, Benjamin Walther, Heshmat Noei, Vedran Vonk, Hauke Heller, Andreas Stierle, and Horst Weller*

Cite This: *J. Phys. Chem. C* 2021, 125, 8224–8235

Read Online

ACCESS | Metrics & More | Article Recommendations | Supporting Information

ABSTRACT: We report on the oxidation and reduction behavior of colloidally stabilized Ni nanoparticles and Pt@NiPt core–shell nanoparticles with a platinum content of 4%. Thin films of both nanoparticle systems were deposited on yttria-stabilized zirconia substrates by spin-coating. Oxidation–reduction cycles were used to remove oxides and organics and obtain metallic particles. The cycling conditions necessary to clean and reduce Pt@NiPt core–shell nanoparticles were milder than for the Ni nanoparticles, which also needed several cycles to burn off residual organics. During cycling, the Ni nanoparticles lost their initially epitaxial relationship with the substrate and adopted a random orientation, while no epitaxial orientation was observable for the core–shell nanoparticles. Reasons for this are discussed together with the influence of platinum on Ni reduction. The Ni and Pt@NiPt nanoparticles sintered during the process but retained crystalline domain diameters close to the original particle diameters. Our results show that colloidally stabilized nanoparticles can be transferred onto a technologically relevant substrate and be reduced to metallic nanoparticles. The fabrication and final structures are discussed as a feasible route to realize solid oxide fuel cell anodes with tailored nickel particle diameter.

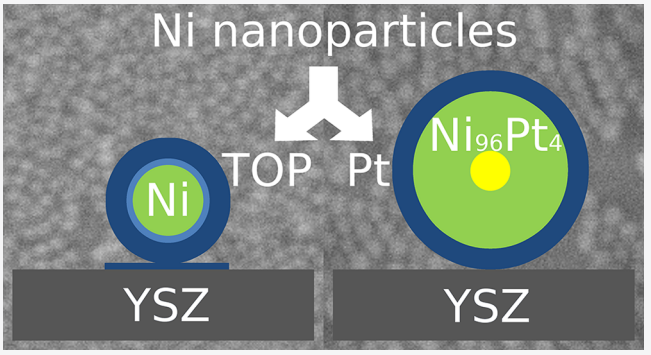

1. INTRODUCTION

Catalytic properties of nanoparticles (NPs) are very closely related to their size,[1−7] whereby there seems to be a general trend that the smaller the better, which ultimately may lead to single-atom catalysis.[8] On the other hand, experimental and theoretical evidence exists that various catalytic properties may peak near a specific size of metallic[9−11] and alloy nanoparticles.[12,13] These examples indicate that many applications would benefit from a tailored nanoparticle size. Here we propose that this could be the case as well for nickel, when used as anode on the solid electrolyte yttria-stabilized zirconia (YSZ) in solid oxide fuel cells (SOFCs). It has been reported that monodisperse Ni NPs with a size of approximately 10 nm show enhanced activity toward a dehydrogenation reaction.[4] At the anode of a SOFC, fuel is being oxidized, which is, in a way, a similar reaction. The chemical processes occurring at the anode of a real device are however much more complex and involve the oxidation and/or hydroxylation of nickel as well.[14] In addition, the microstructure on a much larger length scale of Ni-YSZ cermets, as typically used in SOFCs, plays a role too; the particle and pore sizes may be tuned to optimize the SOFC performance.[15] These examples show that for real SOFCs, the used materials need to be tailored on different length scales. Here we focus on the NP size, which can be related to the intrinsic catalytic activity.

An SOFC electrode is involved in redox cycles, occurring during the activation process and typical working conditions. Pure Ni is prone to oxidation and hydroxylation, both of which may be detrimental to the catalytic and mechanical electrode properties. By alloying Ni with the more noble Pt, the occurrence of NiO and $Ni(OH)_2$ on the surface of the nanoparticles should be suppressed and the nanoparticles should resemble a model system of pure Ni nanoparticles more strongly even at room temperature. Additionally, the response to redox cycling and in particular the reversibility of oxide and hydroxide formation may be improved. To explore this hypothesis, we have studied pure Ni and Pt@NiPt core–shell nanoparticles. The choice for using Ni in SOFCs is primarily based on costs, and therefore we focus our study, as a first step, on using a small amount of 4% of Pt.

To date it is still a challenge to control the synthesis of nanoparticles to achieve the desired properties. In addition, operation of real devices may lead to nanoparticle sintering and

Received: January 27, 2021
Revised: March 26, 2021
Published: April 8, 2021

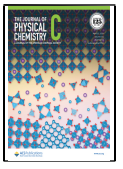

https://doi.org/10.1021/acs.jpcc.1c00762
J. Phys. Chem. C 2021, 125, 8224–8235

with that a loss of their optimum performance.[16] Whereas typical nanoparticle synthesis in gas phase or in solution yields size distributions of about 30%,[17] with the aid of colloids it can be as small as 5%. Monodisperse size distributions such as these are obtained when one short nucleation is followed by a slow growth on the formed nuclei.[18−21] This offers a very interesting route toward tailored nanoparticle properties and allows also for much more detailed basic studies of nanoparticles with a well-defined size. Very common synthesis routes to prepare nickel nanoparticles are based on the chemical reduction of metal salts with $NaBH_4$,[22,23] hydrazine,[24−26] super hydrides,[22] alcohols,[27] and polyols.[28−30] The synthesis method for preparation of nickel nanoparticles with highly narrow size distributions is the thermal decomposition of metal−surfactants complexes with alkyl amines and tri-*n*-octylphosphine followed by reduction in organic solvents with high boiling points.[31−38] The ligands used vary from oleylamine, oleic acid, dioleamide to tri-*n*-octylphosphine.[36,39] A synthesis route to prepare monodisperse spherical alloy nanoparticles is the hot injection (HI) method, where a thermally unstable metal precursor is quickly injected in a hot solution of organic solvents including stabilizing agents such as oleylamine or oleic acid.[40−44]

An important aspect of the use of colloidally stabilized metal NPs for real catalysis applications is the need to lose the ligands. In the case of Ni this is particularly challenging, because it is prone to oxidation and hydroxylation[14] which complicates redox cycling. It is known that Ni particles usually oxidize only partially and that the reduction of the formed NiO is fairly easy. The activation step of real nickel SOFC anodes typically takes place in a hydrogen atmosphere of around 1 mbar and a temperature of 870 K.[45] Much less is known about the mass transport during these gas reactions, in particular when organic ligands are present.

The Ni NPs and Pt@NiPt core−shell nanoparticles studied here offer a chance to investigate the difference in ligand removal for ligands being used in both syntheses such as oleic acid and oleylamine, where differences are more likely attributable to the NP composition and surface. In addition, the use of tri-*n*-octylphosphine (TOP) in the synthesis of the Ni NPs enables the investigation of ligand removal for a ligand known to bond strongly to the surface of Ni.

Here we present a study of the preparation, properties, and behavior under controlled gas atmosphere and elevated temperature of a model solid oxide fuel cell's (SOFC) anode. Pure Ni and Pt@NiPt core−shell nanoparticles (CSNs) have been synthesized using the colloidal stabilization methods of thermal decomposition and HI. By subsequently spin-coating the particles on an yttria-stabilized zirconia substrate, monolayer particle films can be grown. Such planar samples mimic the anode of an SOFC, where the Ni-containing particles catalytically aid fuel consumption and the oxygen-permeable YSZ acts as a solid-state electrolyte.[46]

2. EXPERIMENTAL SECTION

Two different types of nanoparticles are presented in this study: pure Ni NPs and Pt@NiPt core−shell nanoparticles (CSNs). After initial synthesis of the NPs, they were spin-coated onto YSZ substrates. These thin film samples were subsequently annealed under oxidizing and reducing conditions and the NPs composition and structure were characterized by X-ray photoelectron spectroscopy (XPS), X-ray reflectivity (XRR), and X-ray diffraction (XRD). Table 1 summarizes the different conditions used in the oxidation−reduction cycles of the final thin film samples. In the following paragraphs, sample treatments and characterizations are described in detail.

Table 1. Overview of the Oxidation and Reduction Treatments of the Two Different NP Samples[a]

	Ni	Pt@NiPt
annealing in UHV	stepwise up to 1050 K	stepwise up to 700 K
oxidation 1	in air, 3 months	673 K, 1 mbar O_2
oxidation 2	673 K, 1 mbar O_2	
reduction 1	673 K, 1 mbar H_2	923 K, UHV
reduction 2	773 K, 20 mbar H_2	
reduction 3	833 K, 20 mbar H_2	

[a]Due to their different behavior, the two samples have not been subjected to exactly the same conditions in each of the steps.

2.1. Synthesis of Nickel Nanoparticles. Nickel nanoparticles (Ni NPs) were synthesized by thermal decomposition of the organometallic precursor nickel(II) acetylacetonate ($Ni(acac)_2$, 95%, Alfa Aesar) in oleylamine (OAm, 70%, Sigma-Aldrich) in the presence of the ligand tri-*n*-octylphosphine (TOP, 97%, Strem). In a typical procedure,[36] 0.1291 g of $Ni(acac)_2$ (0.50 mmol) was added to 6.9 mL of OAm (21 mmol) and 0.45 mL of TOP (1.0 mmol). The mixture was stirred magnetically under a flow of nitrogen at room temperature (RT) for 20 min to dissolve the solids to give a clear light blue solution. The mixture was further heated to 403 K, maintained for 20 min, and then rapidly heated to 518 K and kept at that temperature for 50 min. After cooling to room temperature, 10 mL of ethanol (EtOH, 100%, VWR Chemicals) was added to the solution to give a black precipitate, which was separated from the solution by centrifugation (10.621 g, 293 K, 10 min). The particles were dissolved in 2 mL of chloroform ($CHCl_3$, ≥99.8%, VWR Chemicals), washed, and separated for the second time by precipitation of the 1:1 mixture of ethanol and methanol (each 10 mL). The obtained nanoparticles were finally dissolved in 2 mL of chloroform, 50 μL of oleylamine, and 25 μL of oleic acid (stock solution; 5.5 g/L nickel).

2.2. Synthesis of Pt@NiPt Core−Shell Nanoparticles. The synthesis method of the CSNs with a platinum core and a nickel platinum alloy shell is briefly described below;[43] a detailed description of the synthesis will be published in another contribution. The chemicals were used without further purification and are listed as follows: nickel(II) acetate tetrahydrate ($Ni(Ac)_2{\cdot}4H_2O$, 99%, Alfa Aesar), platin(II) acetylacetonate ($Pt(acac)_2$, 98%, ABCR), diphenyl ether (DPE, 99%, Sigma-Aldrich), oleylamine (OAm, 98%, Sigma-Aldrich), oleic acid (OAc, 90%, Sigma-Aldrich), 1,2-hexadecanediol (HDD, > 98%, TCI Chemicals), 1,2-dichlorobenzene (DCB, 99%, Acros Organics), tetrahydrofuran (THF, 100%, VWR Chemicals), ethanol (EtOH, 100%, VWR Chemicals), and methanol (MeOH, 99.8%, VWR Chemicals).

In a typical synthesis 0.0275 g of $Ni(Ac)_2{\cdot}4H_2O$ (0.11 mmol), 0.0010 g of HDD (0.0040 mmol), 5 mL of the separately prepared dioleamide ligand (DOA: 2:1 mixture of OAm and OAc) and 5 mL diphenyl ether (31 mmoL) were mixed together. The mixture was stirred magnetically under a flow of nitrogen at 323 K for 5 min to dissolve the solids and obtain a clear light blue solution. The mixture was further heated at 10^{-2} mbar to 353 K and maintained for 30 min to

https://doi.org/10.1021/acs.jpcc.1c00762
J. Phys. Chem. C 2021, 125, 8224−8235

Table 2. Overview of Spin-Coating Recipes for Ni Nanoparticles and Pt@NiPt Core−Shell Nanoparticles on YSZ (111) Substrates

recipe	sample	step	ramp/s	rotation time/s	rotation speed/rpm
I 500 rpm steps	Ni NP	1	1	5	500
		2−3	2	10	1000−1500
		4−5	2	20	2000−2500
		6	2	30	3000
II 250 rpm steps	Pt@NiPt CSN	1−11	1	5	250−2750
		12	1	35	3000

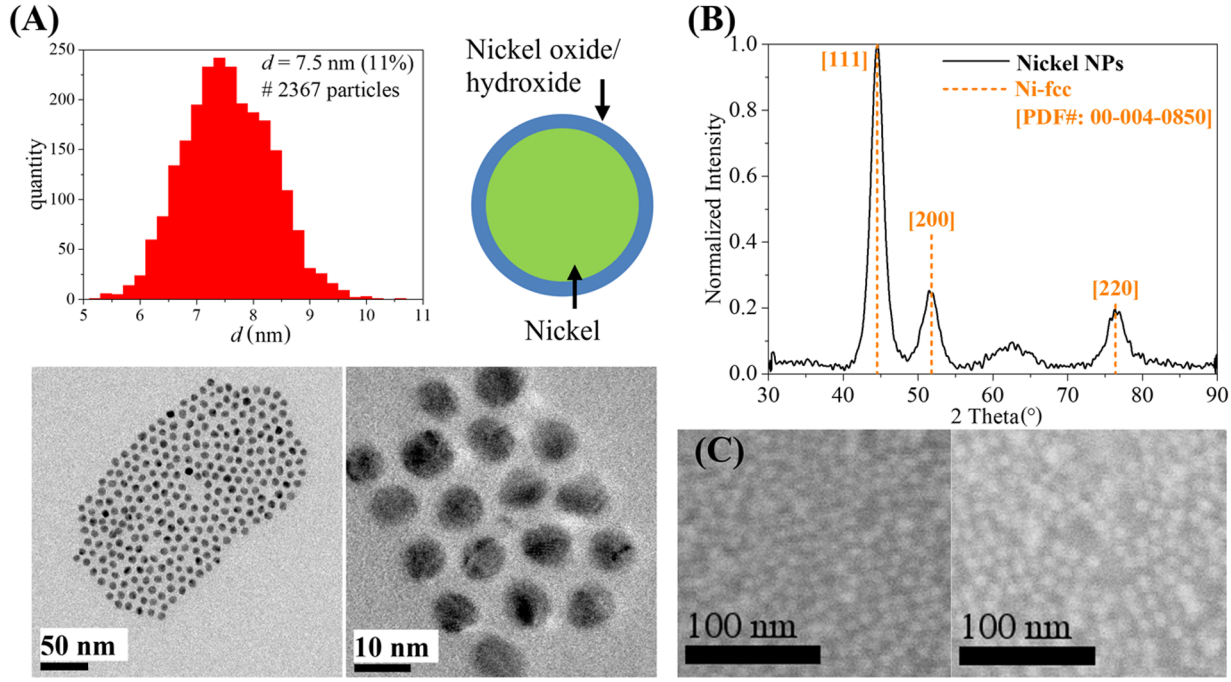

Figure 1. (A) TEM images and size distribution of the nickel NPs produced in oleylamine and 1 mmol of TOP at 518 K. Furthermore, a schematic representation of the particles is shown. (B) Corresponding X-ray diffraction of the nickel nanoparticles. For comparison, the reference reflections of Ni-fcc (orange dotted lines) are given.[50] (C) SEM images of nickel NPs deposited on YSZ (111) substrates appearing in lighter gray and showing the coverage on the edges of the substrate (left) and at its center (right). (Full images appear in SI).

remove oxygen and water, after which a light green, slightly turquoise nickel solution was obtained. Then the solution was heated to 473 K under nitrogen atmosphere, and a pale yellow platinum solution consisting of 0.0016 g of platinum(II) acetylacetonate (0.0040 mmol), 0.10 mL of DCB (0.90 mmol), and 0.30 mL of DPE (1.9 mmol) was injected under vigorous stirring. After the hot injection of the platinum solution, the reaction mixture was stirred for 3 min at 473 K to ensure reproducible conditions at the start of the synthesis. The mixture was then rapidly heated to the reaction temperature of 518 K accompanied by a color change from light green over brown to black and kept at that temperature for 80 min. After reaction, the black dispersion was cooled under nitrogen atmosphere. Ten milliliters of ethanol was added to give a black precipitate, which was separated from the solution by centrifugation (2−16P centrifuge from Sigma; 7.000*g*, room temperature, 10 min). The pale yellow supernatant was discarded, and the nanoparticles were dispersed in 3 mL of THF. They were then washed a second time with 10 mL of methanol followed by centrifugation (10.621*g*, room temperature, 10 min). The nanoparticles were finally dispersed in 3 mL of THF.

2.3. Spin-Coating Procedure of the Nanoparticles on YSZ (111) Substrates. The commercially available YSZ (111) substrates from CrysTec consist of 90.5 mol % zirconium dioxide and 9.5 mol % yttrium oxide (Y_2O_3) and have a miscut of less than 0.1°. The round substrates with a diameter of 10 mm are polished from one side and have a surface area of 78.54 mm^2 and a thickness of 1 mm. The typical rms of the roughness is around 0.2 nm.[47] Various solvents for particle dispersion and different rotational speeds and times were investigated for the coatings (for more information, see SI). Before the particles were coated on the YSZ surfaces, they had to be precipitated with a triple excess volume of ethanol, centrifuged, and then redispersed in 1,2-dichlorobenzene. For the coating, two slightly different rotation sequences were used. The Ni NPs were spin-coated with recipe I and the Pt@NiPt CSNs with recipe II. An overview of the two recipes is summarized in Table 2.

2.4. Characterization. The synthesized nanoparticles were characterized by XRD using a Philips X'Pert PRO MPD diffractometer with Bragg−Brentano geometry and Cu Kα (λ = 1.54 Å) as the incident radiation and high-resolution transmission electron microscopy (HR-TEM) using a Phillips CM 300 UT transmission electron microscope with a 200 kV

https://doi.org/10.1021/acs.jpcc.1c00762
J. Phys. Chem. C 2021, 125, 8224−8235

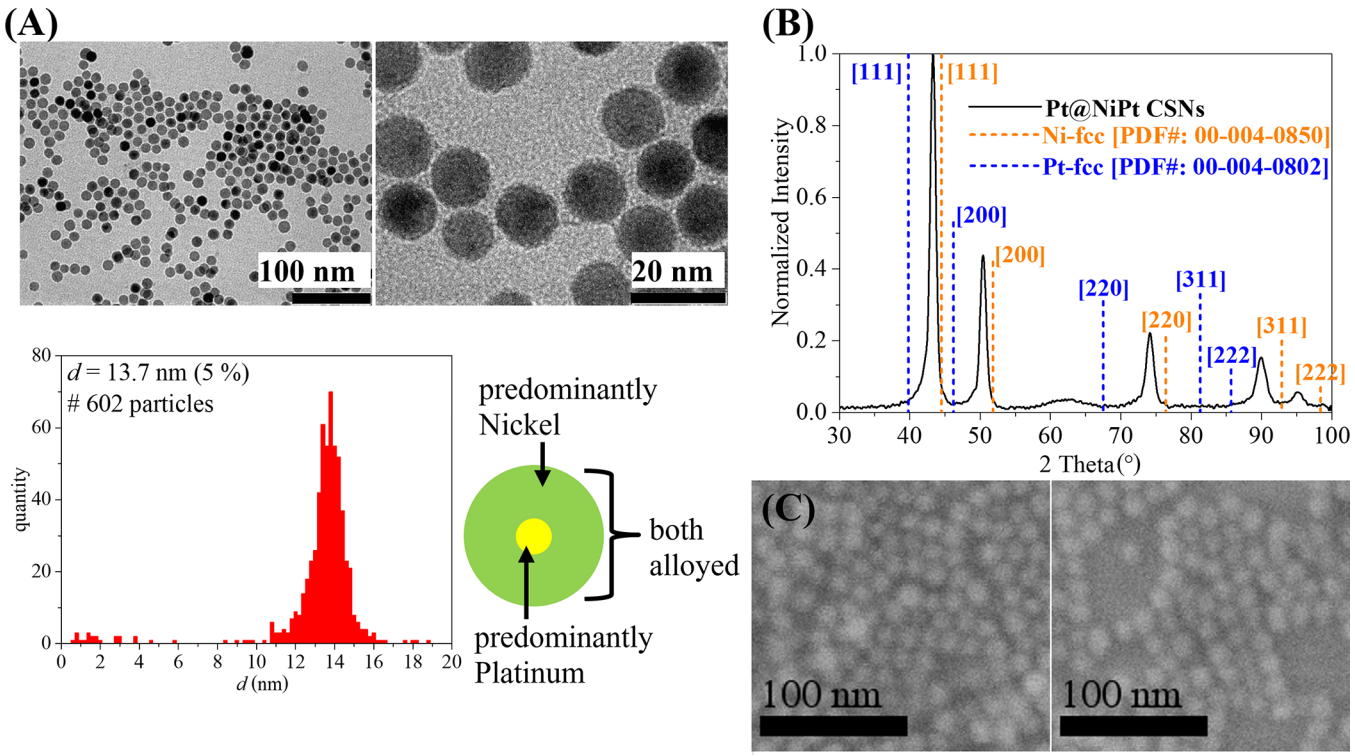

Figure 2. (A) TEM images and size distribution of the Pt@NiPt CSNs produced with a hot injection synthesis using the ligand Dioleamide (DOA) at 518 K. Note small dark spots of ~2 nm diameter in many CSNs. Furthermore, a schematic representation of the CSNs with a platinum-rich core is shown. (B) Corresponding X-ray diffraction of the Pt@NiPt CSNs. For comparison, the reference reflections of Ni-fcc (orange dotted lines) and Pt-fcc (blue dotted lines) are given.[50] (C) SEM images of the coated YSZ substrates showing the NPs in lighter gray. The substrates were coated with Pt@NiPt CSNs following recipe II. SEM images from the edge of the coated substrate (left) and from the center (right) are shown. (Full images appear in SI).

lanthanum hexaboride (LaB_6) filament. For energy-dispersive X-ray spectroscopy (EDX) on the same instrument at 200 kV, an EDAX Silicon drift detector (SDD) was used, and for the evaluation, the Ni-L and Pt-M X-ray lines were used. The particle samples for HR-TEM and EDX were prepared by diluting a freshly washed particle dispersion in toluene until a light brownish solution was obtained, of which 9 μL was then deposited onto a carbon-coated copper grid. The solvent was removed with filter paper.

The surface of the cleaned and particle-coated YSZ (111) substrates was examined by high-resolution scanning electron microscopy (HR-SEM) using a LEO (Zeiss) 1550 Ultra scanning electron microscope with a field emission gun (FEG). The concentration of the stock solutions of the particles was characterized by atomic absorption spectroscopy (AAS) using a PerkinElmer 4100 THGA spectrometer. From each sample a triplicate determination was made. For this purpose, 20−30 μL of the particle dispersion per determination was dried in air, and then the metallic particles were digested in 2 × 4 mL aqua regia under moderate heating (about 60 °C). In the case of Pt@NiPt CSN, 2 mL of perchloric acid had to be added to the aqua regia digestion. After digestion, the clear solution was diluted with Milli-Q water to a total volume of 50 mL and measured.

XPS measurements were carried out using a high-resolution 2D delay line detector at DESY NanoLab.[48] A monochromatic Al Kα X-ray source (photon energy 1486.6 eV; anode operating at 15 kV) was used as incident radiation. XPS spectra were recorded in fixed transmission mode. A pass energy of 25 eV was chosen, resulting in an overall energy resolution better than 0.5 eV. Charging effects were compensated by using a flood gun. The binding energies were calibrated based on the graphitic carbon 1 s peak at 284.8 eV. The XPS setup allows heating the sample, and data are shown up to temperatures of 1050 K. All spectra are recorded at room temperature.

Extended X-ray characterization, consisting of XRR and reciprocal space mapping (RSM), has been performed at the Desy Nanolab.[48] XRR was performed using Mo−Kα radiation and conventional θ−2θ scans, while the RSMs were recorded on a dedicated six-circle diffractometer using Cu−Kα radiation. The nanoparticle-coated YSZ substrates were mounted in a portable UHV chamber, which was used for in situ measurements during annealing and oxidation.

3. RESULTS AND DISCUSSION

3.1. As-Prepared Nickel Nanoparticles and Coating. The diameter of the Ni NPs is 7.5 nm with a standard distribution of 11%. The particles appear nearly spherical, as shown in Figure 1 A. Furthermore, it can be seen in the TEM images and additionally deduced from the X-ray diffractogram in Figure 1 B that the Ni NPs are polycrystalline. The diffraction pattern indicates the existence of pure nickel with the fcc-structure. However, the average diameter of the particles, determined with the Debye−Scherrer[49] equation from the (111) reflex position and the reflex width, is only 3.9 nm, much smaller than when determined from the TEM images. This apparent discrepancy can be explained by considering that only crystalline parts contribute the X-ray diffraction pattern as well as possibly the crystalline volumes

https://doi.org/10.1021/acs.jpcc.1c00762
J. Phys. Chem. C 2021, 125, 8224−8235

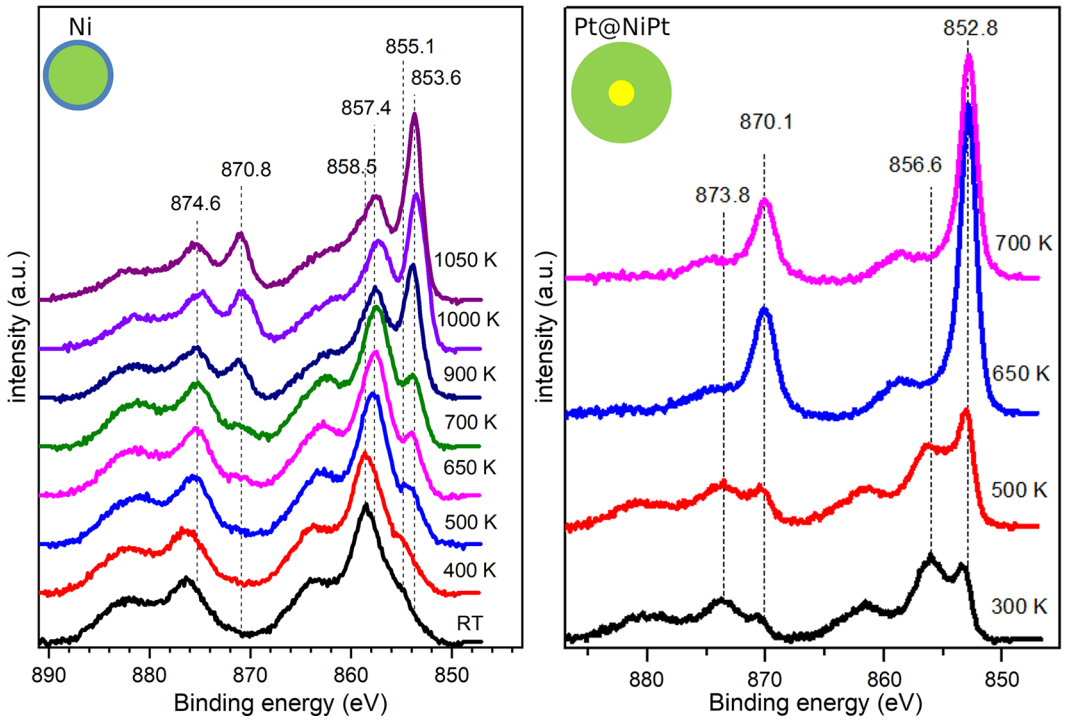

Figure 3. Ni 2p XP spectra taken after deposition of the NPs at room temperature and subsequent annealing to different temperatures as indicated in the figure. (Left) XP spectra taken from the Ni NPs. The spectra are recorded after exposing the sample to air for several days. (Right) XP spectra taken from the Pt@NiPt CSNs.

being polycrystalline fcc nickel. While it seems that the core is highly crystalline the shell consists of less ordered material, such as $Ni(OH)_2$ and NiO, as concluded from the XPS measurements presented hereafter.

The coating of the YSZ substrates with nickel NPs was carried out according to recipe I (see Table 2). After drying, the coated YSZ substrate appeared slightly brownish. The coating was examined by means of SEM. The SEM images are shown in Figure 1C. The coating of the YSZ substrates was slightly more pronounced at the edge than at the center of the substrate. To determine the coverage of the YSZ substrate, the number of particles was manually counted from the SEM images for a defined area of the substrate center (610 × 410 nm). A total of 1011 particles was counted (see full images in SI). It should be noted, however, that manual particle counting is flawed due to the low resolution of the SEM image, the relatively small counted substrate area, and the presence of charge effects. Together with the particle diameter of 7.5 nm, a coverage of the YSZ substrate of 19% was calculated. Because according to the SEM images the coverage further toward the edge of the substrate increased, the total coverage was probably slightly higher.

3.2. As-Prepared Pt@NiPt Core–Shell Nanoparticles and Coating. The diameter as determined from TEM image analysis of the Pt@NiPt CSNs is 13.7 nm with a standard distribution of 5%. The particles are spherical in shape, as can be deduced from Figure 2 A. As with the previously described Ni NPs, the Pt@NiPt CSNs exhibit a partially polycrystalline crystal structure according to the TEM images and the XRD measurements (Figure 2 B).

The diffraction pattern shows narrow reflexes, starting from the nickel reference reflexes, which are slightly shifted to smaller 2θ angles. The resulting d-spacings are a linear combination of pure Pt and Ni, as described by Vegard's law.[51] The composition of the alloy's crystalline part of the particles is determined to be about 26% of platinum. With the Debye–Scherrer equation[49] and the XRD measurements, the particle size can be calculated to be 7.4 nm (σ 16%), which is about half the diameter obtained from the TEM images and indicates a polycrystalline structure. EDX analysis indicates that the total Pt content of the particles is around 4%, much lower than the value obtained by XRD. This seeming discrepancy can be understood by the fact that most of the Pt is situated in the core of the Pt@NiPt CSNs, which may be identified as the small dark spots visible inside the CSN in Figure 2 A. While Figure 2 A also shows a simplified representation of the CSNs with a sharp edge between Pt core and NiPt shell, in reality the Pt content will gradually decrease from the core toward the shell and will not be pure Pt in the core to begin with. The outermost layers will contain very little Pt. Apparently, the crystalline domains contributing most to the diffractogram are richer in Pt and therefore closer to the core. Likely, crystalline domains toward the surface have smaller volumes than further inside as there are not only Ni(Pt) (alloy) phases but NiO phases present as well. As a consequence, they do not show in the diffractogram. The coating of the YSZ substrates with Pt@NiPt CSNs was carried out according to recipe II (see Table 2). After drying, the now-coated YSZ substrate appeared brownish in color, and the coating was examined by means of SEM, which is shown in Figure 2 C.

The coverage of the YSZ substrates with the Pt@NiPt CSNs, as well as the Ni NPs, was slightly higher at the edges than at the center of the substrate. To determine the coverage of the YSZ substrate, the number of particles was manually counted from the SEM images for a defined area of 610 × 410 nm, and 666 particles were counted. Together with the diameter of the CSNs of 13.7 nm, a coverage of 39% was

https://doi.org/10.1021/acs.jpcc.1c00762
J. Phys. Chem. C 2021, 125, 8224–8235

calculated. The increased coverage as compared to the Ni NPs investigated previously may be understood by the ratio of the diameter of the ligand shell determining the interparticle distance to the diameter of the NPs. As the diameter of the ligand shell seems to be comparable for both samples, this ratio decreases drastically for the larger Pt@NiPt CSNs, and they cover a higher share of the YSZ surface. In addition, patches of double and triple layers are more frequent for Pt@NiPt NPs. While this has no influence on the particle counting undertaken here it will become more important when discussing the X-ray reflectivity results.

3.3. XPS: Redox Behavior. The oxidation state of the spin-coated nanoparticles was elucidated by XPS during in situ stepwise annealing. Deconvoluted XP spectra for the RT experiments shown in Figures 3 to 6 appear in SI While performing the experiments, it became clear that the Pt@NiPt core−shell nanoparticles did not need to be subjected to hydrogen atmosphere to be reduced, and the resulting different conditions are listed in Table 1. Figure 3 shows the Ni 2p core level obtained for the pure Ni and Pt@NiPt core−shell nanoparticles.

The Ni 2p peaks in the XP spectrum are dominated by two spin−orbital components of Ni $2p_{3/2}$ and Ni $2p_{1/2}$. At room temperature, one doublet is clearly resolved at 857.5 and 875.0 eV for the pure Ni nanoparticles as well as the satellite peaks at 861.2 and 881.3 eV. Also, a weak doublet is apparent at lower binding energies of the main XP peaks. The doublet peaks at 857.5 and 875.0 eV are attributed to $Ni(OH)_2$. As it is expected, their satellite peaks appeared at higher binding energies than those expected for the NiO or metallic nickel nanoparticles. Between 400 K and 500 K, the Ni 2p peaks of $Ni(OH)_2$ undergo a shift to two new doublets at 856.5 and 874.6 eV and the dominant one at 852.8 and 870.1 eV which indicates the thermal reduction of nickel hydroxide and nickel oxide to metallic nickel, respectively.

The corresponding satellite peaks shift to the lower binding energies and become weaker in intensity. The existence of nickel phosphide can be ruled out because the phosphorus spectra (SI, Figure S3) would then show a particular peak at 129.5 eV,[52] which is not observed in the XP spectra.

Decomposition of nickel hydroxide to metallic nickel also causes a change in the O 1s spectrum. Figure 5 (left) shows a shift of the O 1s peak from 531.4 eV for the $Ni(OH)_2$ to the 530.7 eV attributed to the lattice oxygen of the substrate oxides (ZrO_2 and Y_2O_3).

The Ni 2p core level spectrum of the core−shell particles, see Figure 3 (right), is very different from the Ni 2p core level spectrum at room temperature; however, after annealing, they become more similar. At room temperature, two main doublets were resolved at 852.8 and 870.1 eV and 856.6 and 873.8 eV, attributed to the Ni $2p_{3/2}$ and Ni $2p_{1/2}$ of metallic Ni and NiO species. The satellite peaks appeared at higher binding energies. Unlike the pure Ni nanoparticles, where the reduction started at 600 K but was not completed even at 1050 K, the Pt@NiPt core−shell nanoparticles started being reduced at temperatures as low as 300 K. Further reduction takes place at 500 K, and the Ni were fully reduced in Pt@NiPt CSNs around 650 K (see Figure 3, right). This may be understood by the influence of Pt on the d-band center of Ni. Here the d-band center is expected to be shifted to higher energies, resulting in the Ni reacting more noble.[53] The Ni NPs lose their oxide shell in the temperature range of 700−900 K, while the core−shell particles can be reduced to pure metal already around 500−650 K.

Figure 4 shows the splitting of the Pt 4 $f_{5/2}$ and Pt 4 $f_{7/2}$ peaks at 71.3 and 74.3 eV, attributed to the metallic platinum

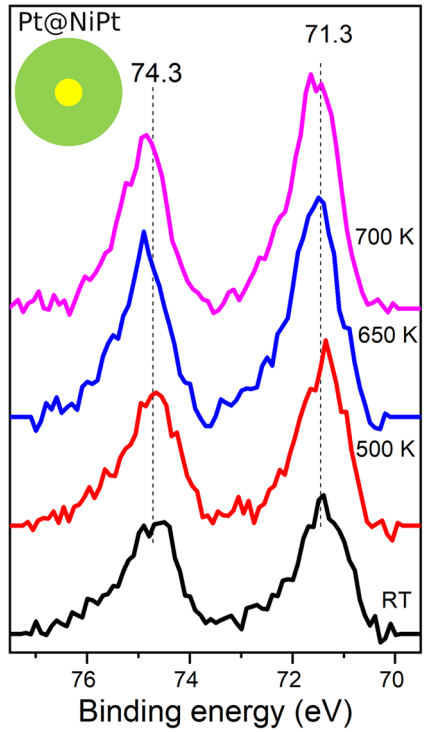

Figure 4. Pt 4f spectra obtained during different stages of annealing the Pt@NiPt particles. The systematic increase of the Pt signal with higher temperature is a consequence of Pt out-diffusion.

obtained after different annealing steps. The Pt signal increased gradually with higher annealing temperatures and/or annealing time. An estimate of the Pt composition is made by comparing the ratio of the Ni 2p and Pt 4f peak areas. This is done by taking the different cross-sections and escape depths explicitly into account. Because the NPs are considerably larger than the photoelectron escape depths of approximately 1 and 2 nm for Ni 2p and Pt 4f respectively, these measurements probe the shell of the NPs. The Pt content increases gradually from 1.8% to 2.9% when the sample is heated from room temperature to 700 K. This indicates that during the vacuum annealing the Pt content throughout the particle becomes more uniform and Pt may segregate to the surface,[54] in line with single-crystal surface investigations.[55] The Pt content in the shell obtained by XPS from the as-received NPs is thus somewhat smaller than the average of about 4% found for the whole particle. This is in accordance with a core−shell structure with a platinum-rich inner core and gradually decreasing platinum content toward the surface.

3.4. XPS: Ligand Shell. To follow the behavior of the organic shell during stepwise annealing, the C 1s spectrum was recorded for the pure Ni sample in Figure 5 (right). The C 1s XP spectrum shows three peaks at 284.8, 285.5, and 288 eV, assigned to the aliphatic C−C, C−O, and C═O, originating from oleic acid or acetylacetonate, respectively. The intensity of all three peaks decreases with an increase in temperature, but the relative intensity changes as well. While the peak at 284.8 eV assigned to aliphatic carbon remains relatively stable,

https://doi.org/10.1021/acs.jpcc.1c00762
J. Phys. Chem. C 2021, 125, 8224−8235

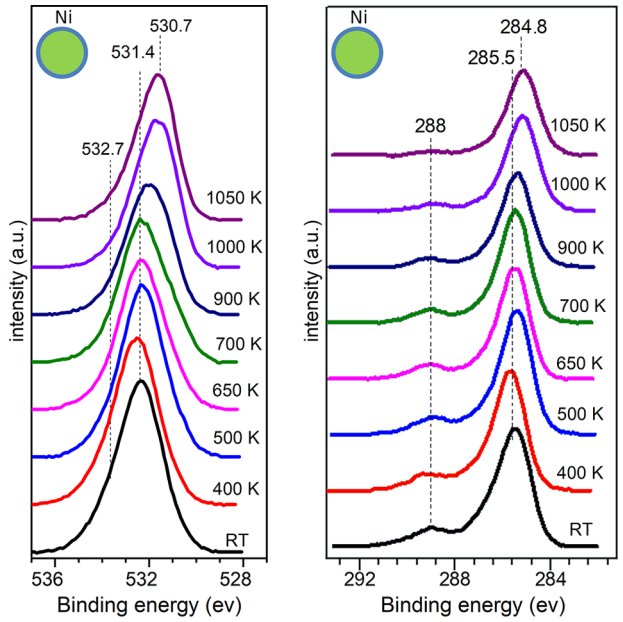

Figure 5. O 1s (left) and C 1s (right) XP spectra of the pure Ni NPs recorded at room temperature after each annealing step as indicated. The details of the peak assignments and temperature development are discussed in the text.

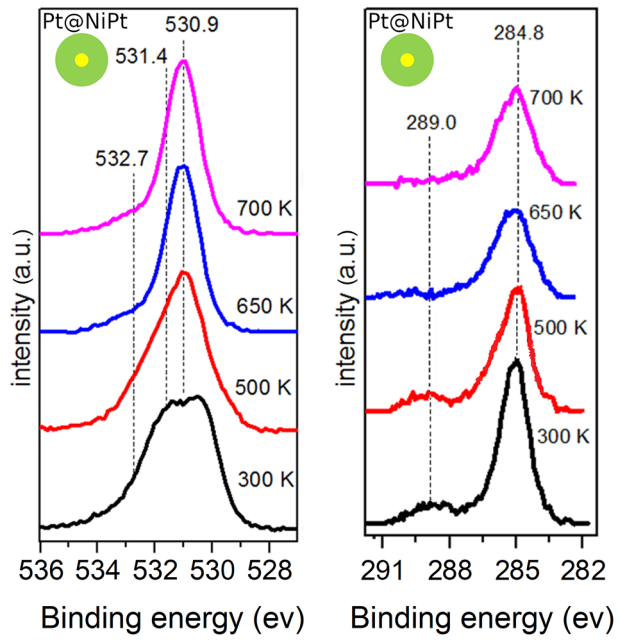

Figure 6. O 1s and C 1s core level spectra of the Pt@NiPt core−shell NPs recorded at room temperature after each annealing step as indicated.

the C═O peak nearly disappears, indicating desorption of oleic acid and acetylacetonate. The corresponding O 1s peak at 532.7 eV disappears as well at 1050 K. This agrees with the values obtained by Dreyer et al., who measured a strong desorption of oleic acid from magnetite nanoparticles at temperatures above 600 K.[56] The highest attainable temperature in the XPS setup together with the UHV conditions is not enough to completely remove the organics. Further oxidation−reduction cycles, using a dedicated sample chamber, were carried out for this purpose.

The O 1s core level spectra shows a doublet at 530.7 and 531.4 eV with similar intensity attributed to the lattice oxygens of the YSZ substrate and NiO, respectively. The C 1s XP spectrum shows one strong peak at 285 eV assigned to the aliphatic carbon chains, and this peak becomes broader and shifts also to lower binding energies around 284.4 eV after annealing, which demonstrates a partial decomposition of the aliphatic carbon chain to other carbonaceous species. However, we did not observe any graphitic carbon or carbide phase in the C 1s region in line with our observations in Pt 4f and Ni 2p core levels. The small peak at 289 eV is attributed to species containing C═O. In the case of Pt@NiPt CSNs, it is not visible anymore at 650 K, showing the desorption and decomposition of C═O-containing species including oleic acid, dioleamide, acetylacetonate, and acetate. In contrast, the C═O peak obtained when measuring Ni NPs was stable up to 1050 K (Figure 5). It likely originated from oleic acid and acetylacetonate at low temperatures and decomposition products thereof at high temperatures. Further studies are needed to understand the interaction of oleic acid and acetylacetonate with oxide substrate (YSZ) and Ni NPs and the mechanism of their stabilization at elevated temperatures. Accordingly, the broad shoulder at about 532.7 eV in the O 1s region vanishes which proves desorption of any carbonyl species (Figure 6).

3.5. X-ray Reflectivity. Figure 7 shows the X-ray reflectivity curves obtained before and after annealing and after an oxidation step of the Ni NPs. The slight oscillations

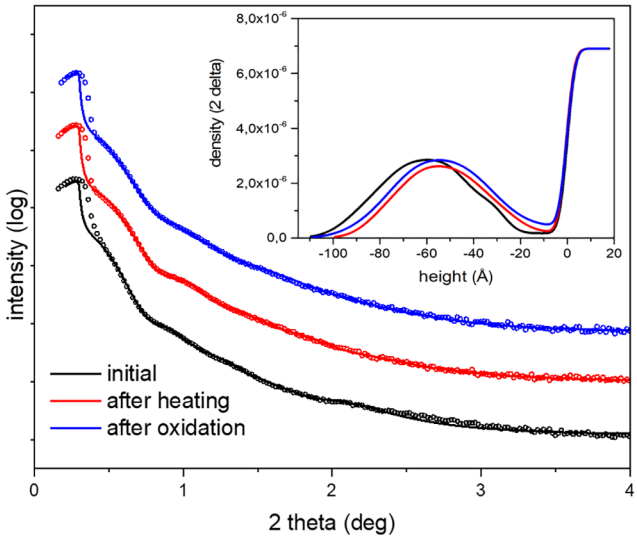

Figure 7. X-ray reflectivity results of the Ni particles spin-coated on an YSZ(111) substrate, showing the intensity (arbitrary units on a logarithmic scale) versus 2θ scattering angle. The different curves have been displaced vertically for clarity. The data shown correlate to the initial state (black circles), after stepwise heating to 1050 K during the XPS measurements (red circles) and after oxidation in air (blue circles). Fits, using a model as described in the text, are shown by the solid lines. The systematic deviation at small incident angles can be explained by more than one-layer-high nanoparticle agglomerates at the border of the samples, only illuminated for small incident angles. The inset shows the electron density profiles fitted to the data. After annealing and oxidation, the average distance of the NPs to the substrate has reduced, which is an indication that the ligand has (partially) disappeared.

https://doi.org/10.1021/acs.jpcc.1c00762
J. Phys. Chem. C 2021, 125, 8224−8235

arise from a nanoparticle-containing layer. By fitting an electron density profile to the experimental data, several structural features are determined, such as the height and coverage of the particles. A slab model was used, whereby for each slab four different parameters are refined: thickness, density, absorption, and roughness. It was found that four independent slabs are needed to obtain a satisfactory fit to the measured XRR curves. Three of these describe the layer of particles, and the fourth is needed to describe the area in between the particles and the substrate, which is systematically found to have a low density, thereby forming a gap only occupied by ligands. The fitted density profile is expressed in values of 2δ, which relates to the real part of the refractive index of the material ($n = 1 - \delta + i\beta$) and which is directly proportional to the electron density, ρ, by

$$\rho = \frac{2\pi\delta}{r_e\lambda^2} \tag{1}$$

with r_e the classical electron radius (2.8×10^{-4} nm) and λ the X-ray wavelength. To rationalize the resulting density distribution, the following simulation is carried out. Assuming a spherical metal particle shape of average diameter d and Gaussian spread σ, the density distribution is calculated. Other parameters that are included are the distance of the particles to the substrate and the density and thickness of the organic shell. The numerically calculated average is shown in Figure 8,

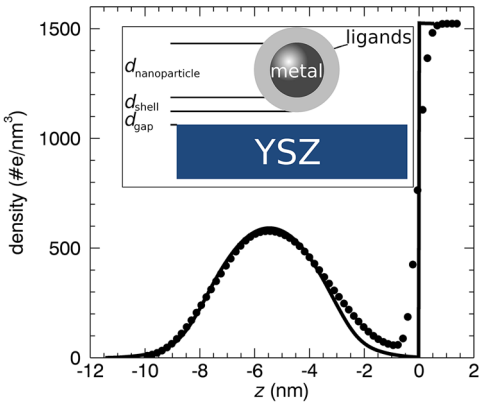

Figure 8. Comparison of the experimentally obtained density profile (dots) from the XRR measurements with a geometrical ball model (black). The parameters used in the model calculation, such as size and its distribution, are listed in Table 3. The inset shows a schematic picture of the spherical NP supported by YSZ and the different distances as listed in Table 3.

together with the curve obtained by XRR. The values are tabulated in Table 3. There is very good agreement between the simulation and the experimentally determined values, especially concerning the shape, as will be shown below. The Ni particle diameters obtained through this method are also in excellent agreement with those obtained by TEM. For the alloy particles, there is a distinct difference in the particle diameter determined by TEM and XRR. Most likely, this is caused by the fact that the geometric model that is used to fit the obtained electron density profile is quite sensitive to the assumed local elemental composition. The estimated diameter might correlate strongly with the exact local composition. The same holds for the estimated total coverage, as discussed below. The Ni NPs' sizes shrink a bit after annealing. In the simulation the organic shell thickness is assumed constant. This implies that any changes in size will be contained in the parameter describing the metal particle size. It seems however most likely that the organic shell shrinks after annealing. At the same time, it is expected that the reduction of oxides and hydroxides will also lead to shrinking. Interestingly, the analysis shows that the metal Ni nanoparticles are not in contact with the substrate but that there exists a gap of very low electron density and approximately 0.5 nm width between them. It might be that it consists of an additional ligand layer containing oleic acid and/or TOP. The Pt@NiPt NPs do not show such an additional organic layer separating the particles from the substrate. This may be understood as a result of the different ligand systems used in the synthesis and stabilization. While the Pt@NiPt CSNs were synthesized with oleylamine and DOA the Ni NPs were synthesized using oleylamine and TOP and further stabilized with oleic acid. Especially oleylamine and to a lesser degree DOA can be removed from the surface of the NPs efficiently. In contrast, TOP may form very stable P−O−Ni bonds[57,58] which likely keep some TOP on the oxidized Ni NPs′ surface, resulting in the observed gap. In addition, phosphor oxide components PO_n are known to inhibit the reduction of NiO, probably due to similar reasons.[59] Finally, also the Pt@NiPt NPs shrink a bit in size after annealing and oxidation, again in line with the assumption that the organic shell disappears to some extent.

A dense Ni layer, fully covering the substrate, would have an electron density of 2570 #e/nm^3. The ratio between the experimentally determined value and that of such a fully covering layer gives the coverage. For the Ni NPs, this results in values around 22−24%, which is in very good agreement with the value obtained from SEM, as the SEM value was determined in the center where the coverage was at its overall minimum, while XRR probes more or less the entire sample.

Table 3. Parameters of the Theoretical Model Used To Calculate the Average Nickel NP Density Distribution along the Interface Normal before and after Heating[a]

	coverage (−)	d (nm)	σ_d (nm)	d_{gap} (nm)	ρ_{metal} (#e/nm^3)	d_{shell} (nm)	ρ_{shell} (#e/nm^3)
Ni							
initial	0.22	7.0	0.0	0.50	560	2.0	213
heated	0.24	6.0	0.0	0.45	628	2.0	213
Pt@NiPt							
initial	0.45[b]	11.2	0.6	∼0	1234	2.0	213
heated	0.47[b]	10.6	0.60	∼0	1301	2.0	213

[a]Listed are the areal coverage, the average NP diameter (d), the Gaussian spread (σ_d), which accounts for the NP size distribution, organic layer thickness (d_{shell}), gap (d_{gap}), and charge density inside the metal nanoparticle (ρ_{metal}) and organic layer (ρ_{shell}). All σ values are normal distributions of their respective value to account for randomness in the layer. [b]Calculated for a Pt content in the 4−7% range.

https://doi.org/10.1021/acs.jpcc.1c00762
J. Phys. Chem. C 2021, 125, 8224−8235

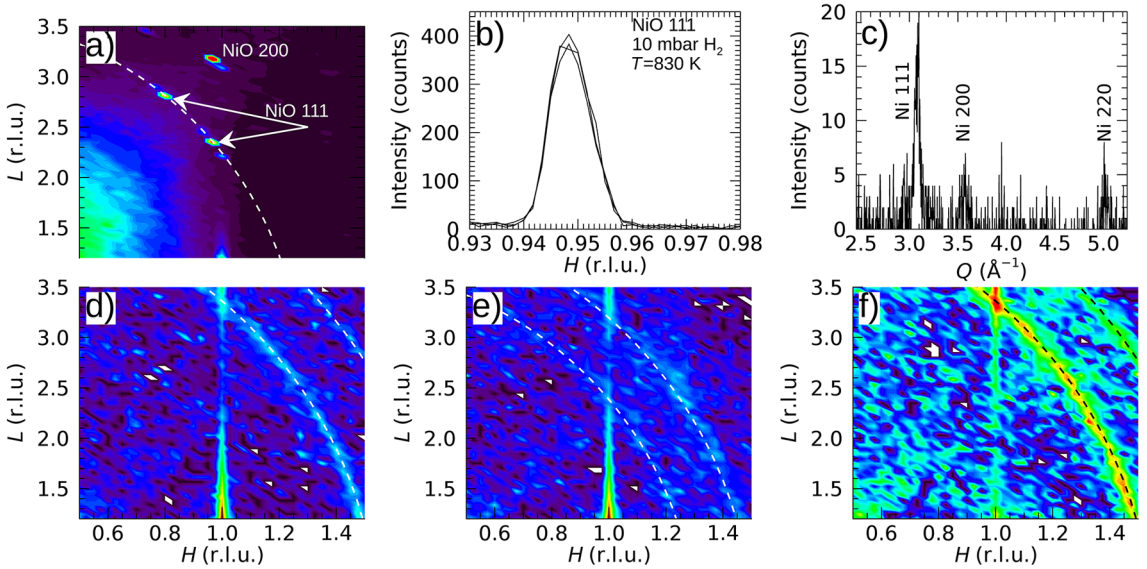

Figure 9. X-ray diffraction results. (a) RSM of the Ni NPs supported by YSZ(111), showing single Bragg reflections belonging to either NiO 111 or 200 reflections and the (faint) substrate (1,0) CTR signal along *L*. The peak indicated by the arrow was measured to be stable during an initial reduction step as indicated in b). The dashed line indicates the ring of constant momentum transfer for the NiO 111 peak[17] and shows at least one other NP orientation to exist besides the 111-oriented NiO NPs. (b) NiO 111 Bragg peak of the oxidized Ni NPs during the initial reduction step at a temperature of 830 K and 10 mbar of H_2. The NPs remained oxidized. (c) Grazing-incidence powder diffraction measurement of the Ni NPs after prolonged oxidation−reduction cycles, showing that eventually pure Ni metal particles formed. The formation of powder rings indicates that the NP orientations changed from being epitaxial to random. (d) RSM of the Pt@NiPt particles after the initial UHV annealing steps during the XPS measurements and reoxidation in air. The particles are not epitaxial and show no oxide but only pure metallic Ni, which again illustrates the protective character of the Pt content. (e) RSM of the Pt@NiPt NPs after oxidation at 670 K and 1 mbar O_2. Only randomly oriented NiO particles have formed. (f) RSM of the Pt@NiPt NPs after a reduction step at 920 K in UHV. The randomly oriented particles have all been reduced again to metallic Ni.

For the Pt@NiPt NPs, a direct comparison with a dense fully covering metal layer suffers from the fact that the exact composition and elemental distribution of the NPs is not known. Assuming a Pt content in the 4−7% range, as discussed above and by using the relation $\rho = c\rho_{Pt} + (1 - c)\rho_{Ni}$ with $\rho_{Ni,Pt}$ the bulk densities of Pt and Ni, and c the concentration, one obtains a coverage in the 45−47% range. Again, taking into account the different uncertainties, the agreement with the coverage of 39% as determined by SEM is rather good.

3.6. Oxidation−Reduction Cycles Followed by in Situ X-ray Diffraction. To further clean and reduce the particles to pure metal, several oxidation−reduction cycles were performed. By oxidizing, the organics should be removed further, and by reduction, the formed oxide again removed. These experiments have been performed in a dedicated mobile UHV chamber which is mounted on a six-circle diffractometer. The sample conditions at the different steps are listed in Table 1.

Figure 9 shows several diffraction patterns obtained for the Ni and Pt@NiPt NPs at different stages. The initial observation of single Bragg reflections in the maps of the Ni nanoparticles shows that they have a well-defined epitaxial relationship with the substrate. Each of the peaks is assigned to belong to NiO, and no reflection was observed from pure Ni. This suggests that the particles are completely oxidized at the beginning of the oxidation−reduction cycles. The XPS data show that after the stepwise annealing under UHV conditions, the particles are partially reduced and some metallic Ni was formed. Apparently, exposing them to air for a long time at room temperature oxidized them completely again. During the first reduction attempts at temperatures up to 830 K and at 10 mbar of H_2, the NiO remained present (Figure 9). Only after many more oxidation−reduction cycles, whereby the H_2 pressure was increased up to 20 mbar, was it possible to obtain metallic Ni particles. Interestingly, during these cycles, the epitaxial relationship between the NPs and substrate got lost and a random orientation was found. This is evidenced by the Debye−Scherrer diffraction rings. The Pt@NiPt core−shell nanoparticles, which already proved to be reducible at lower temperatures during the XPS measurements, showed a random orientation from the start. This sample was not exposed to air for such a long time as that for the Ni NPs and shows only metallic Ni diffraction rings at the beginning of the oxidation−reduction cycles.

Figure 10 shows SEM images of the Ni and Pt@NiPt NPs after all the treatments. In both cases sintering took place. The Ni NPs have grown from an average size of 7.5 nm after preparation to between 16 and 24 nm. The original spherical shape is also lost, which implies the formation and/or growth of certain facets. The Pt@NiPt particles cannot be recognized anymore after all the treatments. For this sample, 100−300 nm large structures have formed, which seem a consequence of coalescence. The fact that in the SEM these islands seem droplike without sharp boundaries may be an indication of their poor crystallinity. This is in line with the XRD measurements which show that for this sample, the underlying crystalline structure has a domain size of about 10 nm. The formed islands are therefore likely formed by smaller randomly oriented crystallites which have coalesced and formed such amorphous structures.

https://doi.org/10.1021/acs.jpcc.1c00762
J. Phys. Chem. C 2021, 125, 8224−8235

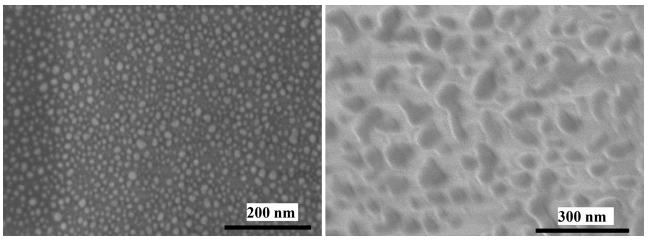

Figure 10. SEM images showing the morphologies of the samples after the oxidation−reduction cycles. (Left) Ni NPs show a diameter between 16 and 24 nm, compared to the initial 7.5 nm (see Figure 1), indicating sintering took place. The shape of the particles has also changed from roughly spherical to having much more pronounced facets. (Right) Pt@NiPt CSNs show massive sintering, whereby coalesced regions of several 100 nm have formed. As seen from the XRD measurements, these larger islands still consist of crystalline building blocks, 10 nm in average size.

4. CONCLUSIONS

Although the two nanoparticle systems investigated in this study differ strongly in their surface composition and properties as well as the ligand system, it was possible to deposit them on the same type of YSZ (111) substrate albeit with differing experimental protocols for spin-coating. The result was the deposition of a near monolayer in both cases, while in the case of Pt@NiPt CSNs, patches of double and triple layers were present, highlighting the versatility of the spin-coating method.

The reducibility of the Ni NPs and Pt@NiPt CSNs as observed by XPS was very different. While Pt@NiPt CSNs were reduced to a metallic state between 500 K and 650 K this was not completely possible for Ni NPs at 1050 K. This can be attributed to several reasons. XPS data showed that the Ni NPs are covered with a significant shell of NiO and $Ni(OH)_2$. At 298 K, the free enthalpy of formation of NiO (−57,3 kJ/mol @ 298 K)[60] is significantly more negative than that of NiPt at 298 K (∼ −9.8 kJ/mol as calculated from Swalin,[61] Wang and Zunger[62]). Therefore, the formation of a NiPt alloy may help with the reduction of the comparably smaller amount of NiO present for Pt@NiPt CSNs to a certain degree as compared to the formation of pure Ni. This acts in concert with the shifting of the Ni d-band center and may contribute to enhanced reducibility of the Pt@NiPt CSNs although the Pt content is rather low at ∼4%. These effects will also be responsible for the lower amount of oxidized Ni species observed after synthesis.

Additionally, NiO reduction may be hindered by the low diffusion coefficient of O, slowing O diffusion to the surface.[63] In this case reoxidation should give hollow spheres if the diameter of the NPs is larger than 5 nm.[64] This was not observed for our NPs with a size of 7.5 nm.

Furthermore, the ligands used are different, and the presence of phosphor, specifically of phosphates,[59] has been shown to inhibit reduction of NiO, possibly due to strong P−O−Ni bonds.[57,58] These bonds may very well form between TOP and NiO and contribute to the weak reducibility of the Ni NPs.

There was also a marked difference in the temperature needed to desorb carbonyl species such as oleic acid from the surface of the NPs. While the temperature needed was 1050 K for the Ni NPs it was 650 K for the Pt@NiPt CSNs, showing very similar behavior as with the reducibility. The bond between Ni/NiO and for example oleic acid should be comparable for both nanoparticle systems, and the fact that it is easier to break in the case of Pt@NiPt CSNs is a sign of the influence the relatively low Pt content is exacting on the behavior of the NPs.

The result of the sintering process was again different for both systems. Here the Ni NPs showed Ni droplets of 16−24 nm diameter while the Pt@NiPt CSNs formed regions of more than 100 nm diameter. This may again be attributed to the influence of the ligands and the stronger bonds that form between carbonyl species such as oleic acid as well as TOP and the surface of the Ni NPs. They will slow down coalescence, as they are only removed at the highest temperatures used during cycling and therefore will still be on the surface to a greater degree than those on the Pt@NiPt CSN surface. The additional layer found between nanoparticles and substrate in the case of Ni NPs may diminish contact between nanoparticles and substrate and therefore strengthen coalescence but does not seem to be the deciding factor in this study. Furthermore, the occurrence of small patches of two or three monolayers in the case of the Pt@PtNi CSNs may facilitate the sintering process.

Finally, the NPs seem to be oriented on the YSZ (111) in the case of Ni NPs while this is not the case for the Pt@NiPt CSNs. This may be attributed to the presence of the double and triple layer patches in the case of Pt@NiPt CSNs. Here the second and third layer CSNs will not have a direct contact to the surface, and therefore an orientation of the Pt@NiPt CSNs of the first layer seems entirely possible and likely.

■ ASSOCIATED CONTENT

Supporting Information

The Supporting Information is available free of charge at https://pubs.acs.org/doi/10.1021/acs.jpcc.1c00762.

SEM images of the supported YSZ substrates, XP spectra of P 2p at room temperature and annealing to up to 1050 K, and deconvoluted XP spectra at room temperature (PDF)

■ AUTHOR INFORMATION

Corresponding Author

Horst Weller − *Department of Chemistry, University of Hamburg, 20146 Hamburg, Germany; Fraunhofer Center for Applied Nanotechnology, 20146 Hamburg, Germany;* orcid.org/0000-0003-2967-6955; Email: Horst.Weller@chemie.uni-hamburg.de

Authors

Vivien Gutknecht − *Department of Chemistry, University of Hamburg, 20146 Hamburg, Germany;* orcid.org/0000-0002-7638-1618

Benjamin Walther − *Deutsches Elektronen-Synchrotron (DESY), 22607 Hamburg, Germany*

Heshmat Noei − *Deutsches Elektronen-Synchrotron (DESY), 22607 Hamburg, Germany;* orcid.org/0000-0003-1294-3527

Vedran Vonk − *Deutsches Elektronen-Synchrotron (DESY), 22607 Hamburg, Germany;* orcid.org/0000-0001-9854-1101

Hauke Heller − *Department of Chemistry, University of Hamburg, 20146 Hamburg, Germany;* orcid.org/0000-0002-5857-5558

Andreas Stierle − *Deutsches Elektronen-Synchrotron (DESY), 22607 Hamburg, Germany; Fachbereich Physik, Universität*

Hamburg, 20355 Hamburg, Germany; orcid.org/0000-0002-0303-6282

Complete contact information is available at: https://pubs.acs.org/10.1021/acs.jpcc.1c00762

Author Contributions

The manuscript was written through contributions of all authors. All authors have given approval to the final version of the manuscript.

Notes

The authors declare no competing financial interest.

■ ACKNOWLEDGMENTS

This research was funded by the Deutsche Forschungsgemeinschaft (DFG, German Research Foundation)—Projektnummer 192346071—SFB 986, projects A1, A7. We gratefully acknowledge financial support by the Federal Ministry for Economic Affairs and Energy (BMWi) due to an enactment of the German Bundestag under grant no. 03ET1435B (HiKAB).

■ ABBREVIATIONS

NPs, nanoparticles; YSZ, yttria-stabilized zirconia; SOFCs, solid oxide fuel cells; HI, hot injection; CSNs, core−shell nanoparticles; XPS, X-ray photoelectron spectroscopy; XRR, X-ray reflectivity; XRD, X-ray diffraction; OAm, oleylamine; TOP, tri-*n*-octylphosphine; OAc, oleic acid; DPE, diphenyl ether; HDD, 1,2-hexadecanediol; DCB, 1,2-dichlorobenzene; THF, tetrahydrofuran; DOA, dioleamide; EDX, energy-dispersive X-ray spectroscopy; SDD, silicon drift detector; HR-SEM, high-resolution scanning electron microscopy; FEG, field emission gun; AAS, atomic absorption spectroscopy; RSM, reciprocal space mapping; RT, room temperature

■ REFERENCES

(1) Hou, Z.; Gao, J.; Guo, J.; Liang, D.; Lou, H.; Zheng, X. Deactivation of Ni catalysts during methane autothermal reforming with CO_2 and O_2 in a fluidized-bed reactor. *J. Catal.* **2007**, *250* (2), 331−341.

(2) Guisbiers, G.; Abudukelimu, G.; Hourlier, D. Size-dependent catalytic and melting properties of platinum-palladium nanoparticles. *Nanoscale Res. Lett.* **2011**, *6* (1), 396.

(3) Wilson, O. M.; Knecht, M. R.; Garcia-Martinez, J. C.; Crooks, R. M. Effect of Pd Nanoparticle Size on the Catalytic Hydrogenation of Allyl Alcohol. *J. Am. Chem. Soc.* **2006**, *128* (14), 4510−4511.

(4) Guo, K.; Li, H.; Yu, Z. Size-Dependent Catalytic Activity of Monodispersed Nickel Nanoparticles for the Hydrolytic Dehydrogenation of Ammonia Borane. *ACS Appl. Mater. Interfaces* **2018**, *10* (1), 517−525.

(5) Zhou, X.; Xu, W.; Liu, G.; Panda, D.; Chen, P. Size-Dependent Catalytic Activity and Dynamics of Gold Nanoparticles at the Single-Molecule Level. *J. Am. Chem. Soc.* **2010**, *132* (1), 138−146.

(6) Suchomel, P.; Kvitek, L.; Prucek, R.; Panacek, A.; Halder, A.; Vajda, S.; Zboril, R. Simple size-controlled synthesis of Au nanoparticles and their size-dependent catalytic activity. *Sci. Rep.* **2018**, *8* (1), 4589.

(7) Li, J.; Chen, W.; Zhao, H.; Zheng, X.; Wu, L.; Pan, H.; Zhu, J.; Chen, Y.; Lu, J. Size-dependent catalytic activity over carbon-supported palladium nanoparticles in dehydrogenation of formic acid. *J. Catal.* **2017**, *352*, 371−381.

(8) Wang, A.; Li, J.; Zhang, T. Heterogeneous single-atom catalysis. *Nature Reviews Chemistry* **2018**, *2* (6), 65−81.

(9) Valden, M.; Lai, X.; Goodman, D. W. Onset of Catalytic Activity of Gold Clusters on Titania with the Appearance of Nonmetallic Properties. *Science* **1998**, *281* (5383), 1647.

(10) Heiz, U.; Sanchez, A.; Abbet, S.; Schneider, W. D. Catalytic Oxidation of Carbon Monoxide on Monodispersed Platinum Clusters: Each Atom Counts. *J. Am. Chem. Soc.* **1999**, *121* (13), 3214−3217.

(11) Tritsaris, G. A.; Greeley, J.; Rossmeisl, J.; Nørskov, J. K. Atomic-Scale Modeling of Particle Size Effects for the Oxygen Reduction Reaction on Pt. *Catal. Lett.* **2011**, *141* (7), 909−913.

(12) Goto, S.; Hosoi, S.; Arai, R.; Tanaka, S.; Umeda, M.; Yoshimoto, M.; Kudo, Y. Particle-Size- and Ru-Core-Induced Surface Electronic States of Ru-Core/Pt-Shell Electrocatalyst Nanoparticles. *J. Phys. Chem. C* **2014**, *118* (5), 2634−2640.

(13) Hernandez-Fernandez, P.; Masini, F.; McCarthy, D. N.; Strebel, C. E.; Friebel, D.; Deiana, D.; Malacrida, P.; Nierhoff, A.; Bodin, A.; Wise, A. M.; et al. Mass-selected nanoparticles of PtxY as model catalysts for oxygen electroreduction. *Nat. Chem.* **2014**, *6* (8), 732−738.

(14) Sarantaridis, D.; Atkinson, A. Redox Cycling of Ni-Based Solid Oxide Fuel Cell Anodes: A Review. *Fuel Cells* **2007**, *7* (3), 246−258.

(15) Suzuki, T.; Hasan, Z.; Funahashi, Y.; Yamaguchi, T.; Fujishiro, Y.; Awano, M. Impact of Anode Microstructure on Solid Oxide Fuel Cells. *Science* **2009**, *325* (5942), 852.

(16) Gates, B. C. Supported Metal Clusters: Synthesis, Structure, and Catalysis. *Chem. Rev.* **1995**, *95* (3), 511−522.

(17) Vonk, V.; Khorshidi, N.; Stierle, A. Structure and Oxidation Behavior of Nickel Nanoparticles Supported by YSZ(111). *J. Phys. Chem. C* **2017**, *121* (5), 2798−2806.

(18) Sun, S.; Murray, C. B. Synthesis of monodisperse cobalt nanocrystals and their assembly into magnetic superlattices (invited). *J. Appl. Phys.* **1999**, *85* (8), 4325−4330.

(19) Murray, C. B.; Kagan, C. R.; Bawendi, M. G. Synthesis and Characterization of Monodisperse Nanocrystals and Close-Packed Nanocrystal Assemblies. *Annu. Rev. Mater. Sci.* **2000**, *30* (1), 545−610.

(20) Murray, C. B.; Kagan, C. R.; Bawendi, M. G. Self-Organization of CdSe Nanocrystallites into Three-Dimensional Quantum Dot Superlattices. *Science* **1995**, *270* (5240), 1335.

(21) Peng, X.; Wickham, J.; Alivisatos, A. P. Kinetics of II-VI and III-V Colloidal Semiconductor Nanocrystal Growth: "Focusing" of Size Distributions. *J. Am. Chem. Soc.* **1998**, *120* (21), 5343−5344.

(22) Hou, Y.; Kondoh, H.; Ohta, T.; Gao, S. Size-controlled synthesis of nickel nanoparticles. *Appl. Surf. Sci.* **2005**, *241* (1), 218−222.

(23) Nouneh, K.; Oyama, M.; Diaz, R.; Abd-Lefdil, M.; Kityk, I. V.; Bousmina, M. Nanoscale synthesis and optical features of metallic nickel nanoparticles by wet chemical approaches. *J. Alloys Compd.* **2011**, *509* (19), 5882−5886.

(24) Chen, D.-H.; Hsieh, C.-H. Synthesis of nickel nanoparticles in aqueous cationic surfactant solutions. *J. Mater. Chem.* **2002**, *12* (8), 2412−2415.

(25) Wu, Z. G.; Munoz, M.; Montero, O. The synthesis of nickel nanoparticles by hydrazine reduction. *Adv. Powder Technol.* **2010**, *21* (2), 165−168.

(26) Jeon, Y.; Lee, G. H.; Park, J.; Kim, B.; Chang, Y. Magnetic Properties of Monodisperse NiHx Nanoparticles and Comparison to Those of Monodisperse Ni Nanoparticles. *J. Phys. Chem. B* **2005**, *109* (25), 12257−12260.

(27) Huaman, J. L. C.; Hironaka, N.; Tanaka, S.; Shinoda, K.; Miyamura, H.; Jeyadevan, B. Size-controlled monodispersed nickel nanocrystals using 2-octanol as reducing agent. *CrystEngComm* **2013**, *15* (4), 729−737.

(28) Zhang, X.; Yin, H.; Cheng, X.; Jiang, Z.; Zhao, X.; Wang, A. Modifying effects of polyethylene glycols and sodium dodecyl sulfate on synthesis of Ni nanocrystals in 1,2-propanediol. *Appl. Surf. Sci.* **2006**, *252* (23), 8067−8072.

(29) Tzitzios, V.; Basina, G.; Gjoka, M.; Alexandrakis, V.; Georgakilas, V.; Niarchos, D.; Boukos, N.; Petridis, D. Chemical synthesis and characterization of hcp Ni nanoparticles. *Nanotechnology* **2006**, *17* (15), 3750−3755.

(30) Couto, G. G.; Klein, J. J.; Schreiner, W. H.; Mosca, D. H.; de Oliveira, A. J. A.; Zarbin, A. J. G. Nickel nanoparticles obtained by a modified polyol process: Synthesis, characterization, and magnetic properties. *J. Colloid Interface Sci.* **2007**, *311* (2), 461−468.
(31) Carenco, S.; Boissière, C.; Nicole, L.; Sanchez, C.; Le Floch, P.; Mézailles, N. Controlled Design of Size-Tunable Monodisperse Nickel Nanoparticles. *Chem. Mater.* **2010**, *22* (4), 1340−1349.
(32) Davar, F.; Fereshteh, Z.; Salavati-Niasari, M. Nanoparticles Ni and NiO: Synthesis, characterization and magnetic properties. *J. Alloys Compd.* **2009**, *476* (1), 797−801.
(33) Park, J.; Kang, E.; Son, S. U.; Park, H. M.; Lee, M. K.; Kim, J.; Kim, K. W.; Noh, H. J.; Park, J. H.; Bae, C. J.; et al. Monodisperse Nanoparticles of Ni and NiO: Synthesis, Characterization, Self-Assembled Superlattices, and Catalytic Applications in the Suzuki Coupling Reaction. *Adv. Mater.* **2005**, *17* (4), 429−434.
(34) Mourdikoudis, S.; Simeonidis, K.; Vilalta-Clemente, A.; Tuna, F.; Tsiaoussis, I.; Angelakeris, M.; Dendrinou-Samara, C.; Kalogirou, O. Controlling the crystal structure of Ni nanoparticles by the use of alkylamines. *J. Magn. Magn. Mater.* **2009**, *321* (18), 2723−2728.
(35) Pan, Y.; Jia, R.; Zhao, J.; Liang, J.; Liu, Y.; Liu, C. Size-controlled synthesis of monodisperse nickel nanoparticles and investigation of their magnetic and catalytic properties. *Appl. Surf. Sci.* **2014**, *316*, 276−285.
(36) Chen, Y.; Peng, D.-L.; Lin, D.; Luo, X. Preparation and magnetic properties of nickel nanoparticles via the thermal decomposition of nickel organometallic precursor in alkylamines. *Nanotechnology* **2007**, *18* (50), 505703.
(37) LaGrow, A. P.; Ingham, B.; Cheong, S.; Williams, G. V. M.; Dotzler, C.; Toney, M. F.; Jefferson, D. A.; Corbos, E. C.; Bishop, P. T.; Cookson.; et al. Synthesis, Alignment, and Magnetic Properties of Monodisperse Nickel Nanocubes. *J. Am. Chem. Soc.* **2012**, *134* (2), 855−858.
(38) Murray, C. B.; Sun, S.; Doyle, H.; Betley, T. Monodisperse 3d Transition-Metal (Co,Ni,Fe) Nanoparticles and Their Assembly intoNanoparticle Superlattices. *MRS Bull.* **2001**, *26* (12), 985−991.
(39) Kraynov, A.; Müller, T. E. Concepts for the Stabilization of Metal Nanoparticles in Ionic Liquids. *Applications of Ionic Liquids in Science and Technology*; IntechOpen, 2011.
(40) Shevchenko, E. V.; Talapin, D. V.; Rogach, A. L.; Kornowski, A.; Haase, M.; Weller, H. Colloidal Synthesis and Self-Assembly of $CoPt_3$ Nanocrystals. *J. Am. Chem. Soc.* **2002**, *124* (38), 11480−11485.
(41) Sun, S.; Murray, C. B.; Weller, D.; Folks, L.; Moser, A. Monodisperse FePt Nanoparticles and Ferromagnetic FePt Nanocrystal Superlattices. *Science* **2000**, *287* (5460), 1989.
(42) Sun, S.; Anders, S.; Thomson, T.; Baglin, J. E. E.; Toney, M. F.; Hamann, H. F.; Murray, C. B.; Terris, B. D. Controlled Synthesis and Assembly of FePt Nanoparticles. *J. Phys. Chem. B* **2003**, *107* (23), 5419−5425.
(43) Ahrenstorf, K.; Albrecht, O.; Heller, H.; Kornowski, A.; Görlitz, D.; Weller, H. Colloidal Synthesis of $NixPt_{1-x}$ Nanoparticles with Tuneable Composition and Size. *Small* **2007**, *3* (2), 271−274.
(44) Rao, C. R. K.; Trivedi, D. C. Chemical and electrochemical depositions of platinum group metals and their applications. *Coord. Chem. Rev.* **2005**, *249* (5), 613−631.
(45) Jeangros, Q.; Aebersold, A. B.; Hébert, C.; Van Herle, J.; Hessler-Wyser, A. A TEM study of Ni interfaces formed during activation of SOFC anodes in H_2: Influence of grain boundary symmetry and segregation of impurities. *Acta Mater.* **2016**, *103*, 442−447.
(46) Wang, W.; Su, C.; Wu, Y.; Ran, R.; Shao, Z. Progress in Solid Oxide Fuel Cells with Nickel-Based Anodes Operating on Methane and Related Fuels. *Chem. Rev.* **2013**, *113* (10), 8104−8151.
(47) Vonk, V.; Khorshidi, N.; Stierle, A.; Dosch, H. Atomic structure and composition of the yttria-stabilized zirconia (111) surface. *Surf. Sci.* **2013**, *612*, 69−76.
(48) Stierle, A. K.; Keller, T. F.; Noei, H.; Vonk, V.; Röhlsberger, R. DESY NanoLab. *JLSRF* **2016**, *2*, 1−9.
(49) Scherrer, P. Bestimmung Der Größe Und Der Inneren Struktur von Kolloidteilchen Mittels Röntgenstrahlen. *Nachrichten von der Gesellschaft der Wissenschaften zu Göttingen, Math. Klasse* **1918**, *26*, 98−100.
(50) Swanson, H. E. Standard X-Ray Diffraction Powder Patterns. *Natl. Bur. Stand. (U. S.)* **1953**, *Circ. 539* (13), 106.
(51) Denton, A. R.; Ashcroft, N. W. Vegard's law. *Phys. Rev. A: At., Mol., Opt. Phys.* **1991**, *43* (6), 3161−3164.
(52) Cecilia, J. A.; Infantes-Molina, A.; Rodríguez-Castellón, E.; Jiménez-López, A. A novel method for preparing an active nickel phosphide catalyst for HDS of dibenzothiophene. *J. Catal.* **2009**, *263* (1), 4−15.
(53) Hammer, B.; Nørskov, J. K. Electronic factors determining the reactivity of metal surfaces. *Surf. Sci.* **1995**, *343* (3), 211−220.
(54) Wang, G.; Van Hove, M. A.; Ross, P. N.; Baskes, M. I. Monte Carlo simulations of segregation in Pt-Ni catalyst nanoparticles. *J. Chem. Phys.* **2005**, *122* (2), 024706.
(55) Hofer, W. Surface segregation of PtNi alloys — comparing theoretical and experimental results. *Fresenius' J. Anal. Chem.* **1993**, *346* (1), 246−251.
(56) Dreyer, A.; Feld, A.; Kornowski, A.; Yilmaz, E. D.; Noei, H.; Meyer, A.; Krekeler, T.; Jiao, C.; Stierle, A.; Abetz, V.; et al. Organically linked iron oxide nanoparticle supercrystals with exceptional isotropic mechanical properties. *Nat. Mater.* **2016**, *15* (5), 522−528.
(57) Murali Krishna, G.; Gandhi, Y.; Veeraiah, N. NiO-induced crystallization and optical characteristics of $Li_2O−CaF_2−P_2O_5$ glass system. *Phys. Status Solidi A* **2008**, *205* (1), 177−187.
(58) Johnson, B.; Chand, N. R. K.; Sudhakar, B. K.; Srinivasa Rao, G. Chemical durability, thermal stability and spectroscopic studies of the influence of Ni^{2+} ions in oxyfluorophosphate glasses. *J. Mater. Sci.: Mater. Electron.* **2016**, *27* (8), 8833−8847.
(59) Sakitani, K.; Nakamura, K.-i.; Ikenaga, N.-o.; Miyake, T.; Suzuki, T. Oxidative Dehydrogenation of Ethane over NiO-loaded High Surface Area ZrO_2 Catalysts. *J. Jpn. Pet. Inst.* **2010**, *53* (6), 327−335.
(60) Boyle, B. J.; King, E. G.; Conway, K. C. Heats of Formation of Nickel and Cobalt Oxides (NiO and CoO) of Combustion Calorimetry. *J. Am. Chem. Soc.* **1954**, *76* (14), 3835−3837.
(61) Swalin, R. A. *Thermodynamics of Solids*, 2nd ed.; Wiley-VCH: New York, 1972.
(62) Wang, L. G.; Zunger, A. Why are the 3d-5d compounds CuAu and NiPt stable, whereas the 3d-4d compounds CuAg and NiPd are not. *Phys. Rev. B: Condens. Matter Mater. Phys.* **2003**, *67* (9), 092103.
(63) Chenna, S.; Banerjee, R.; Crozier, P. A. Atomic-Scale Observation of the Ni Activation Process for Partial Oxidation of Methane Using In Situ Environmental TEM. *ChemCatChem* **2011**, *3* (6), 1051−1059.
(64) Railsback, J. G.; Johnston-Peck, A. C.; Wang, J.; Tracy, J. B. Size-Dependent Nanoscale Kirkendall Effect During the Oxidation of Nickel Nanoparticles. *ACS Nano* **2010**, *4* (4), 1913−1920.

https://doi.org/10.1021/acs.jpcc.1c00762
J. Phys. Chem. C 2021, 125, 8224−8235